

Spin-orbit induced hole spin relaxation in InAs and GaAs quantum dots

J.I. Clemente, C. Segarra, and J. Planelles*

Departament de Química Física i Analítica, Universitat Jaume I, Castelló de la Plana, Spain

(Dated: December 2, 2024)

We study the effect of valence band spin-orbit interactions on the acoustic phonon assisted spin relaxation of holes confined in quantum dots. Heavy hole-light hole ($hh-lh$) mixing and all the spin-orbit terms arising from zinc-blende bulk inversion asymmetry (BIA) are considered on equal footing in a fully 3D Hamiltonian. We show that $hh-lh$ mixing and BIA have comparable contributions to the hole spin relaxation in self-assembled QDs, but BIA becomes dominant in gated QDs. The dependence of the hole spin relaxation on the QD geometry and spin splitting energy is drastically different from that of electrons, with a non-monotonic behavior which results from the interplay between SOI terms. Our results reconcile contradictory predictions of previous theoretical works and are consistent with experiments.

PACS numbers: 73.21.La,71.70.Ej,72.25Rb,63.20.kd

I. INTRODUCTION

In the last years, the spin of holes confined in III-V semiconductor quantum dots (QDs) has emerged as a promising building block for spintronic and spin-based quantum information devices.¹ As compared to electrons, the *p*-like nature of the hole orbitals leads to weaker hyperfine interaction with the lattice nuclei, resulting in coherence times which hold promise for applications.^{2–7} As a matter of fact, demonstrations of hole spin manipulation in QDs have been recently reported^{8–10} and theoretical proposals of control mechanisms are being proposed.^{11–14} In this context, the study of hole spin relaxation has become a subject of interest. Hole spin relaxation is also important for optical applications because it is believed to rule the exciton spin dynamics in both dark-to-bright exciton transitions^{15–18} –which affect exciton storage times^{19–21}– and transitions within the bright doublet²² –which affect light depolarization¹⁷–.

Experimental observations in self-assembled InAs QDs point at hole spin lifetimes ranging from $T_1^h \sim 10$ ps to $T_1^h \sim 1$ ms.^{2,23–26} The large dispersion is partly attributed to the different relaxation mechanism involved in different studies. When the energy splitting between orthogonal spin states is small, hyperfine interaction is the dominant relaxation channel.^{16,27} In this case, the lifetime is strongly dependent on the degree of $hh-lh$ mixing. If the hole state is a pure hh , as in the ground state of flat (quasi-2D) QDs, the hyperfine interaction takes an Ising form and spin relaxation is slow, but it rapidly increases in non-flat QDs due to $hh-lh$ mixing.^{1,7} On the other hand, when the energy splitting exceeds the nuclear magnetic field, the valence band spin-orbit interaction (SOI) takes over as the main source of relaxation.^{16,27} Long hole spin lifetimes have then been observed, reaching up to $T_1^h \sim 0.25$ ms, which is only 5–10 times shorter than electron spin lifetimes, T_1^e .²⁶ This result is encouraging for the use of holes in quantum information and optical applications, but it is surprising because the valence band SOI interaction is known to be much stronger than that of the conduction band.²⁸

The above paradox has prompted a number of theoretical works trying to understand which factors determine the relaxation dynamics of single holes under magnetic fields^{29–33} and that of holes forming excitons^{15,22,34,35} in quasi-2D InAs/GaAs QDs. For the relaxation to take place one needs a source of energy relaxation, which in these systems is provided by the acoustic phonon bath,^{23,24} plus a source of spin admixture. Woods et al.²⁹ and Lu et al.³⁰ proposed that the latter is the coupling between hh and lh subbands. Other authors have suggested instead that the splitting between hh and lh subbands in flat QDs is large owing to confinement and strain, so that spin admixture must be due to other SOI mechanisms. It was then proposed that hole SOI should have a similar origin to that of conduction electrons, namely the BIA of zinc-blende crystals, which gives rise to Dresselhaus SOI terms.²⁸ Bulaev and Loss assumed the cubic-in-*k* Dresselhaus term is dominant and showed that T_1^h could then become comparable to T_1^e in flat QDs.³¹ Other studies followed this assumption and succeeded in explaining some experimental observations.^{15,26,32} By contrast, Tsitsishvili et al. suggested that if the lateral confinement is weak, it is the linear-in-*k* term that dominates the mixing.³⁵ Last, Roszak et al.³⁴ suggested that for holes forming excitons it is the electron-hole (*e-h*) exchange interaction together with the strain that gives rise to hole spin admixture.

It is worth noting that all the previous works assumed a dominating SOI mechanism without actually comparing with others. In addition, simplified models disregarding $hh-lh$ mixing become highly parametric, and different parameters were needed to explain different experimental observations even in the same system.^{15,26,32} The lack of a comprehensive study translates into many open questions which show that hole spin relaxation in QDs is still not fully understood. To name a few: (i) while Ref. 29 predicts that T_1^h decreases with the QD diameter, Ref. 30 predicts exactly the opposite behavior; (ii) Ref. 31 predicted $T_1^h > T_1^e$ in the limit of 2D QDs, but experiments on self-assembled QDs have only shown $T_1^e/T_1^h = 5 - 10$,²⁶ so that one wonders if any

realistic QD structure would actually permit holes relaxing slower than electrons; (iii) in excitons, the role of $e\text{-}h$ exchange energy is not clear: while experiments with self-assembled QDs have shown negligible dependence of T_1^h ,²⁴ a strong dependence has been found in colloidal quantum rods.³⁶

In this work, we aim at covering the existing gap in the understanding of hole spin relaxation in QDs. We study the hole spin dynamics considering simultaneously $hh\text{-}lh$ mixing and all the different Dresselhaus SOI terms arising from the BIA of zinc-blende crystals, along with the hole-acoustic phonon coupling. All the terms are described within a four-band $k\text{-}p$ formalism and 3D Hamiltonians, which allows us to provide a general overview on the effect of the QD size and geometry dependence while relying on well-known bulk parameters only. In this way, we are able to establish the regime of validity of previous studies which assumed a single dominating SOI mechanism. Furthermore, we explore spheroidal QDs beyond the usual quasi-2D limit, thus providing theoretical assessment for developing experimental research with spherical and prolate QDs.^{18,36}

We find that $hh\text{-}lh$ is the main SOI channel in prolate or spherical QDs, but Dresselhaus SOI has a comparable contribution in oblated QDs (such as self-assembled dots), and it becomes dominant in quasi-2D QDs with very weak confinement (as in electrostatically confined dots). The competition between SOI coupling terms and the energy splitting between hh and lh leads to a non-monotonic dependence of T_1^h with the QD geometry, in sharp contrast with the well-known case of electrons. This explains the opposite trends reported by different theoretical studies in the literature. The dependence of T_1^h on the electron-hole exchange energy we predict is consistent with experiments on colloidal nanorods³⁶, but it suggests that two-phonon processes are relevant in self-assembled QDs. In prolate QDs, where the ground state is formed by lh , the spin relaxation is shown to take place in similar timescales as for transitions between hh states. However, the coupling to acoustic phonons is different, with deformation potential interaction being the main mechanism even for vanishing spin splitting energy.

II. THEORETICAL MODEL

We study the spin relaxation of holes confined in zinc blende QDs grown along the [001] direction. The hole spin states are considered split energetically, for example by the $e\text{-}h$ exchange interaction in excitons or any other source that can be viewed as an effective axial magnetic field. Thus, similar results can be expected for transitions between Zeeman sublevels under moderate external magnetic fields.

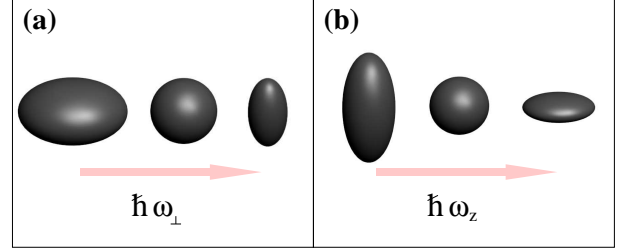


FIG. 1: Geometry of QDs with varying lateral (a) and vertical (b) confinement frequency.

A. Hamiltonian

The system Hamiltonian reads:

$$H = H_h + H_{ph} + H_{h-ph}. \quad (1)$$

In Eq. (1), H_h is the hole Hamiltonian,

$$H_h = H_L + H_{BIA} + V_{QD} \mathcal{I} + H_Z, \quad (2)$$

where H_L is the 4-band Luttinger Hamiltonian describing the coupled $hh\text{-}lh$ bands.³⁷ It includes quadratic terms in k only:

$$H_L = \frac{1}{m_0} \left[\left(\gamma_1 + \frac{5}{2} \gamma_2 \right) \frac{k^2}{2} - \gamma_2 (k_x^2 J_x^2 + k_y^2 J_y^2 + k_z^2 J_z^2) - 2\gamma_3 (\{k_x, k_y\} \{J_x, J_y\} + \{k_y, k_z\} \{J_y, J_z\} + \{k_z, k_x\} \{J_z, J_x\}) \right] \quad (3)$$

where m_0 is the free electron mass, γ_i are the Luttinger parameters, $k_j = -i \hbar \partial_j$ the j component of the linear momentum, $\{A, B\} = \frac{1}{2}(AB + BA)$ and J_i is the i -th component of the angular momentum corresponding to the quantum number $J = 3/2$. To get the matrix representation of this hamiltonian we multiply the first term of equation (3) by the 4×4 unit matrix and employ the standard matrix representation of the $J = 3/2$ components of the angular momentum.³⁸ We finally get:

$$H_L = \begin{pmatrix} P+Q & -S & R & 0 \\ -S^\dagger & P-Q & 0 & R \\ R^\dagger & 0 & P-Q & S \\ 0 & R^\dagger & S^\dagger & P+Q \end{pmatrix}, \quad (4)$$

with

$$P = \frac{1}{2m_0} \gamma_1 (k_x^2 + k_y^2 + k_z^2), \quad (5)$$

$$Q = \frac{1}{2m_0} \gamma_2 (k_x^2 + k_y^2 - 2k_z^2), \quad (6)$$

$$R = \frac{1}{2m_0} \left[-\sqrt{3} \gamma_2 (k_x^2 - k_y^2) + 2i\sqrt{3} \gamma_3 k_x k_y \right] \quad (7)$$

$$S = \frac{1}{2m_0} 2\sqrt{3} \gamma_3 (k_x - i k_y) k_z. \quad (8)$$

H_{BIA} includes the linear and the Dresselhaus SOI third order in k terms:²⁸

$$\begin{aligned} H_{BIA} = & \frac{2}{\sqrt{3}} C_k [k_x \{J_x, J_y^2 - J_z^2\} + \text{cp}] \\ & + b_{41} (\{k_x, k_y^2 - k_z^2\} J_x + \text{cp}) \\ & + b_{42} (\{k_x, k_y^2 - k_z^2\} J_x^3 + \text{cp}) \\ & + b_{51} (\{k_x, k_y^2 + k_z^2\} \{J_x, J_y^2 - J_z^2\} + \text{cp}) \\ & + b_{52} (k_x^3 \{J_x, J_y^2 - J_z^2\} + \text{cp}), \end{aligned} \quad (9)$$

where C_k , b_{41} , b_{42} , b_{51} and b_{52} are material dependent coefficients and cp stands for cyclic permutations of the preceding terms. The matrix form of the Hamiltonian terms above is given in the Appendix. One can notice that all BIA terms provide direct mixing between hh spin up and spin down ($J_z = +3/2$ and $J_z = -3/2$) components except for b_{41} , which requires the participation of the lh ($J_z = +1/2$ and $J_z = -1/2$) components. Rashba SOI is neglected in this study because for holes in QDs it is inefficient.³¹ V_{QD} describes the confining potential of the QD. We model QDs with parabolic confinement in the x , y and z directions,

$$V_{QD} = -\frac{1}{2} \chi_{\perp} (x^2 + y^2) - \frac{1}{2} \chi_z z^2 \quad (10)$$

where χ_{\perp} and χ_z are the force constants perpendicular and parallel to the growth direction, respectively. Eq. (10) allows us to simulate 3D spheroidal QDs with different aspect ratios, from flat (quasi-2D) to spherical or elongated (quasi-1D) structures, see Fig. 1. H_Z is the Hamiltonian modeling the splitting of the hole states by an effective axial magnetic field, three times larger for heavy ($|J_z| = 3/2$) than for light holes ($|J_z| = 1/2$). This field could originate e.g. from the $e\text{-}h$ exchange interaction³⁴ or a spin Zeeman effect. Then, we assume that:

$$H_Z = \frac{1}{2} \begin{pmatrix} \Delta & 0 & 0 & 0 \\ 0 & \frac{1}{3}\Delta & 0 & 0 \\ 0 & 0 & -\frac{1}{3}\Delta & 0 \\ 0 & 0 & 0 & -\Delta \end{pmatrix}. \quad (11)$$

To calculate the hole states from H_h , we note that the diagonal terms correspond to harmonic oscillator Hamiltonians:

$$\begin{aligned} P + Q + V_{QD} = & T_{hh,\perp} - \frac{1}{2} \chi_{\perp} (x^2 + y^2) \\ & + T_{hh,z} - \frac{1}{2} \chi_z z^2, \end{aligned} \quad (12)$$

and

$$\begin{aligned} P - Q + V_{QD} = & T_{lh,\perp} - \frac{1}{2} \chi_{\perp} (x^2 + y^2) \\ & + T_{lh,z} - \frac{1}{2} \chi_z z^2, \end{aligned} \quad (13)$$

where $T_{i,j} = \frac{\hbar^2}{2m_j^i} k_j^2$, with $i = (hh, lh)$, $j = (\perp, z)$, $k_{\perp} = (k_x^2 + k_y^2)^{1/2}$, $m_{\perp}^{hh} = m_0/(\gamma_1 + \gamma_2)$, $m_z^{hh} = m_0/(\gamma_1 - 2\gamma_2)$,

$m_{\perp}^{lh} = m_0/(\gamma_1 - \gamma_2)$, and $m_z^{lh} = m_0/(\gamma_1 + 2\gamma_2)$. This suggests rewriting all derivatives and coordinates of H_h in terms of harmonic oscillator ladder operators and then projecting it onto a basis formed by oscillator eigenstates. The problem is that Eq. (12) has hh masses while Eq. (13) has lh masses, and hence they have different oscillator frequency, $\omega_j^i = (\chi_j/m_j^i)^{1/2}$. Because the off-diagonal terms of H_L couple hh and lh components, it is convenient to use a single kind of oscillator states, e.g. hh states. This can be done by rewriting Eq. (13) in terms of the hh harmonic oscillator Hamiltonians:

$$\begin{aligned} P - Q + V_{QD} = & \frac{\gamma_1 - \gamma_2}{\gamma_1 + \gamma_2} H_{hh,\perp} - \frac{\gamma_2}{\gamma_1 + \gamma_2} \chi_{\perp} (x^2 + y^2) \\ & + \frac{\gamma_1 + 2\gamma_2}{\gamma_1 - 2\gamma_2} H_{hh,z} + \frac{2\gamma_2}{\gamma_1 - 2\gamma_2} \chi_z z^2, \end{aligned} \quad (14)$$

where $H_{hh,\perp} = T_{hh,\perp} - \chi_{\perp} (x^2 + y^2)/2$ and $H_{hh,z} = T_{hh,z} - \chi_z (z^2)/2$. The resulting hole states are Luttinger spinors of the form:

$$|\Psi_m^h\rangle = \sum_{r,J_z} c_{r,J_z}^m |v_x, v_y, v_z\rangle |3/2, J_z\rangle, \quad (15)$$

where $v_j = 0, 1, 2 \dots$ is the quantum number of the 1D hh harmonic oscillator along the j direction, r is the combined orbital quantum number, $r = (v_x, v_y, v_z)$ and $|3/2, J_z\rangle$ the Bloch function.

H_{ph} in Eq. (1) is the Hamiltonian of acoustic phonons, given by $H_{ph} = \sum_{\mathbf{q}\lambda} \hbar \omega_{q\lambda} a_{\mathbf{q}\lambda}^{\dagger} a_{\mathbf{q}\lambda}$, with $\omega_{q\lambda}$ standing for the phonon energy spectrum of branch λ ($\lambda = l, t1, t2$ for longitudinal and the two transversal phonon modes) and momentum \mathbf{q} . We restrict to low phonon energies, where the linear dispersion regime applies, $\omega_{q\lambda} = c_{\lambda} q$, with c_{λ} as the phonon velocity.

H_{h-ph} is the hole-phonon interaction,

$$H_{h-ph} = e \phi_{pz} \mathcal{I} + H_{dp}, \quad (16)$$

where e is the hole charge, ϕ_{pz} the piezoelectric potential and H_{dp} the deformation potential term. These are the two relevant scattering mechanisms at low temperatures.³⁰ The piezoelectric potential is given by:³⁹

$$\begin{aligned} \phi_{pz} = & \sum_{\lambda} \phi_{pz}^{\lambda} = \\ & - \sum_{\lambda \mathbf{q}} \frac{4\pi i}{\epsilon_r q^2} h_{14} (q_x \varepsilon_{yz}^{\lambda} + q_y \varepsilon_{zx}^{\lambda} + q_z \varepsilon_{xy}^{\lambda}). \end{aligned} \quad (17)$$

where ϵ_r is the relative dielectric constant, h_{14} the piezoelectric constant and ε_{ij} the strain tensor component. On the other hand, the deformation potential term is given by the Bir-Pikus strain Hamiltonian:

$$\mathcal{H}_{dp} = \sum_{\lambda} \begin{pmatrix} p^{\lambda} + q^{\lambda} & -s^{\lambda} & r^{\lambda} & 0 \\ -(s^{\lambda})^{\dagger} & p^{\lambda} - q^{\lambda} & 0 & r^{\lambda} \\ (r^{\lambda})^{\dagger} & 0 & p^{\lambda} - q^{\lambda} & s \\ 0 & (r^{\lambda})^{\dagger} & (s^{\lambda})^{\dagger} & p^{\lambda} + q^{\lambda} \end{pmatrix}, \quad (18)$$

where:

$$p^\lambda = -a(\varepsilon_{xx}^\lambda + \varepsilon_{yy}^\lambda + \varepsilon_{zz}^\lambda), \quad (19)$$

$$q^\lambda = -\frac{b}{2}(\varepsilon_{xx}^\lambda + \varepsilon_{yy}^\lambda - 2\varepsilon_{zz}^\lambda), \quad (20)$$

$$r^\lambda = \frac{\sqrt{3}}{2}b(\varepsilon_{xx}^\lambda - \varepsilon_{yy}^\lambda) - id\varepsilon_{xy}^\lambda, \quad (21)$$

$$s^\lambda = -d(\varepsilon_{zx}^\lambda - i\varepsilon_{yz}^\lambda). \quad (22)$$

Here a , b and d are the valence band deformation potential constants.

The components of the strain tensor are rewritten using normal-modes coordinates,²⁹

$$\varepsilon_{ij}^\lambda = -\frac{i}{2} \sum_{\mathbf{q}} U^\lambda(q) (\eta_\lambda^i(\mathbf{q}) q_j + \eta_\lambda^j(\mathbf{q}) q_i) F(\mathbf{q}, \mathbf{r}), \quad (23)$$

where $F(\mathbf{q}, \mathbf{r}) = (e^{-i\mathbf{qr}} a_q^+ + e^{i\mathbf{qr}} a_q)$ and $U^\lambda(q) = \sqrt{\hbar/2\rho V \omega_{q\lambda}}$, with ρ and V standing for the crystal density and volume. $\eta_\lambda(\mathbf{q})$ are the phonon polarization vectors: $\eta_l(\mathbf{q}) = (q_x, q_y, q_z)/q$, $\eta_{t1}(\mathbf{q}) = (q_x q_z, q_y q_z, -q_\perp^2)/q q_\perp$ and $\eta_{t2}(\mathbf{q}) = (q_y, -q_x, 0)/q_\perp$, with $q_\perp = \sqrt{q_x^2 + q_y^2}$. The piezoelectric potential now reads:

$$\begin{aligned} \phi_{pz}^l &= -\frac{12\pi h_{14}}{\epsilon_r} U^l(q) \sum_{\mathbf{q}} \frac{q_x q_y q_z}{q^3} F(\mathbf{q}, \mathbf{r}), \\ \phi_{pz}^{t1} &= -\frac{4\pi h_{14}}{\epsilon_r} U^t(q) \sum_{\mathbf{q}} \frac{q_x q_y (2q_z^2 - q_\perp^2)}{q^3 q_\perp} F(\mathbf{q}, \mathbf{r}), \\ \phi_{pz}^{t2} &= -\frac{4\pi h_{14}}{\epsilon_r} U^t(q) \sum_{\mathbf{q}} \frac{q_z (q_y^2 - q_x^2)}{q^2 q_\perp} F(\mathbf{q}, \mathbf{r}), \end{aligned} \quad (24)$$

In turn, the deformation potential operators become:

$$\begin{aligned} p^l &= i a U^l(q) \sum_{\mathbf{q}} q F(\mathbf{q}, \mathbf{r}), \\ q^l &= i \frac{b}{2} U^l(q) \sum_{\mathbf{q}} \left(q - 3 \frac{q_z^2}{q} \right) F(\mathbf{q}, \mathbf{r}), \\ r^l &= -i U^l(q) \sum_{\mathbf{q}} \left(\frac{\sqrt{3}}{2} b \frac{q_x^2 - q_y^2}{q} - id \frac{q_x q_y}{q} \right) F(\mathbf{q}, \mathbf{r}), \\ s^l &= i d U^l(q) \sum_{\mathbf{q}} \frac{q_z (q_x - i q_y)}{q} F(\mathbf{q}, \mathbf{r}), \end{aligned} \quad (25)$$

for longitudinal phonons,

$$\begin{aligned} p^{t1} &= 0, \\ q^{t1} &= i \frac{b}{2} U^t(q) \sum_{\mathbf{q}} \left(\frac{3 q_z q_\perp}{q} \right) F(\mathbf{q}, \mathbf{r}), \\ r^{t1} &= -i U^t(q) \sum_{\mathbf{q}} \left(\frac{\sqrt{3}}{2} b \frac{q_z (q_x^2 - q_y^2)}{q q_\perp} - id \frac{q_x q_y q_z}{q q_\perp} \right) \\ &\quad F(\mathbf{q}, \mathbf{r}), \\ s^{t1} &= i \frac{d}{2} U^t(q) \sum_{\mathbf{q}} \frac{(q_z^2 - q_\perp^2) (q_x - i q_y)}{q_\perp q} F(\mathbf{q}, \mathbf{r}), \end{aligned} \quad (26)$$

for transversal $t1$ phonons, and

$$\begin{aligned} p^{t2} &= 0, \\ q^{t2} &= 0, \\ r^{t2} &= -i U^t(q) \sum_{\mathbf{q}} \left(\sqrt{3} b \frac{q_x q_y}{q_\perp} - id \frac{q_y^2 - q_x^2}{2 q_\perp} \right) \\ &\quad F(\mathbf{q}, \mathbf{r}), \\ s^{t2} &= -\frac{d}{2} U^t(q) \sum_{\mathbf{q}} \frac{q_z (q_x - i q_y)}{q_\perp} F(\mathbf{q}, \mathbf{r}), \end{aligned} \quad (27)$$

for transversal $t2$ phonons.

B. Relaxation rate

We calculate the spin relaxation from an initial hole state $|\Psi_i^h\rangle$, with energy E_i^h , to a final hole state $|\Psi_f^h\rangle$ with energy E_f^h . The relaxation rate is estimated with a Fermi golden rule. We consider zero temperature, so that there is no phonon absorption. After integrating over phonon degrees of freedom, the rate is given by:

$$\tau_{i \rightarrow f}^{-1} = \frac{2\pi}{\hbar} \sum_{\lambda, \mathbf{q}} \left| \langle \Psi_f^h | \mathcal{H}_{h-ph}^{\lambda q} | \Psi_i^h \rangle \right|^2 \delta(\Delta E_{fi} + \hbar c_\lambda q). \quad (28)$$

Here $\mathcal{H}_{h-ph}^{\lambda q}$ is the hole-phonon interaction Hamiltonian, Eq. (16), but for a fixed phonon branch λ and momentum \mathbf{q} , and $\Delta E_{fi} = E_f^h - E_i^h$. It can be seen from Eqs. (24-27) that all the terms of $\mathcal{H}_{h-ph}^{\lambda q}$ contain a factor which depends on \mathbf{q} only and $F(\mathbf{q}, \mathbf{r})$, which depends on spatial coordinates as well. Thus, when expanded, the matrix element $\langle \Psi_f^h | \mathcal{H}_{h-ph}^{\lambda q} | \Psi_i^h \rangle$ takes the form:

$$\langle \Psi_f^h | \mathcal{H}_{h-ph}^{\lambda q} | \Psi_i^h \rangle = \sum_{J'_z, J_z, r', r} (c_{r', J'_z}^f)^* c_{r, J_z}^i M_{J'_z, J_z}^\lambda(\mathbf{q}) G_{r', r}(\mathbf{q}). \quad (29)$$

where $G_{r', r}(\mathbf{q}) = \langle r' | e^{-i\mathbf{qr}} | r \rangle$ and $M_{J'_z, J_z}^\lambda(\mathbf{q})$ gathers the \mathbf{q} -dependent factor of the $\mathcal{H}_{h-ph}^{\lambda q}$ term coupling J_z and J'_z . $G_{r', r}(\mathbf{q})$ is calculated analytically using iterative procedures as described in Ref. 40. The sum over \mathbf{q} in Eq. (28) is then carried out using numerical integration. To this end, it is convenient to use spherical coordinates, as the modulus q is fixed by the resonance condition and we are left with a two-dimensional integral.

Calculations are carried out for InAs QDs embedded in a GaAs matrix. When differences are expected, we also calculate GaAs QD embedded in an $\text{Al}_x\text{Ga}_{1-x}\text{As}$ matrix. Table I summarizes the parameters we use. The parameters correspond to the QD material, except for the crystal density and velocity of sound, which correspond to the matrix material because we assume bulk phonons (for simplicity, for $\text{Al}_x\text{Ga}_{1-x}\text{As}$ we assume $x \rightarrow 0$ and use GaAs phonon parameters). For the dielectric constant, an average value of $\epsilon_r = 12.9$ is taken all over the

TABLE I: Parameters used in the numerical calculations for InAs (left column) and GaAs (right column) QDs. GaAs parameters are used for the matrix in both cases. e^- , h^+ and ph stand for electron, hole and phonon.

Parameter	Symbol	InAs	GaAs	Ref.
e^- mass (m_0)	m_e	0.026	0.067	41
h^+ Luttinger param.	γ_1	20	6.98	41
h^+ Luttinger param.	γ_2	8.5	2.06	41
h^+ Luttinger param.	γ_3	9.2	2.93	41
e^- deformation pot. (eV)	a_c	-5.08	-7.17	41
h^+ deformation pot. (eV)	a	1.0	1.16	41
h^+ deformation pot. (eV)	b	-1.8	-2.0	41
h^+ deformation pot. (eV)	c	-3.6	-4.8	41
e^- BIA coeff. (eV·Å ³)	b_{41}^e	27.18	27.58	28
h^+ BIA coeff. (eV·Å)	C_k	-0.0112	-0.0034	28
h^+ BIA coeff. (eV·Å ³)	b_{41}^h	-50.18	-81.93	28
h^+ BIA coeff. (eV·Å ³)	b_{42}^h	1.26	1.47	28
h^+ BIA coeff. (eV·Å ³)	b_{51}^h	0.42	0.49	28
h^+ BIA coeff. (eV·Å ³)	b_{52}^h	-0.84	-0.98	28
Longitudinal ph speed (m/s)	c_l	4720	4720	41
Transversal ph speed (m/s)	c_t	3340	3340	41
Crystal density (kg/m ³)	ρ	5310	5310	41
Piezoelectric coeff. (V/cm)	h_{14}	$3.5 \cdot 10^6$	$1.45 \cdot 10^7$	49

structure. The basis used to solve Hamiltonian (1) contains all the hh oscillator eigenstates with the quantum numbers $v_x, v_y < 13$ and $v_z < 9$.

III. NUMERICAL RESULTS AND DISCUSSION

We shall start this section by describing the dependence of the hole spin lifetime on the QD geometry and the spin splitting magnitude (Section III A). The influence of each parameter can be understood by analyzing the spin admixture mechanisms, as we show in Section III B. Next, in Section III C, we study the effect of the ground state changing from mainly hh character, which is the case addressed in most previous studies, to mainly lh character. This transition is observed in QDs with large aspect ratio.⁴²⁻⁴⁵ Last, in Section III D, we compare the role of deformation potential and piezoelectric potential interactions in determining the efficiency of hole-phonon coupling.

A. Geometry and spin splitting dependence

Solid lines in Figure 2 show the hole spin lifetime as a function of the QD geometry and the spin splitting energy of InAs QDs. For comparison, we also plot the electron spin lifetimes (dotted lines). The latter have been calculated using the same formalism as for holes but adapted for single-band conduction electrons.⁴⁰ Both electrons and holes are assumed to feel the same force constant, but we use the hh oscillator frequency, ω_z^{hh} or ω_{\perp}^{hh} , to denote the confinement strength (for simplicity,

we shall often drop the hh superscript). One can see immediately in the figure that the behavior of holes differs drastically from the well-known case of electrons. Below we summarize the influence of each parameter.

Fig. 2(a) shows the spin lifetime dependence on the lateral confinement in QDs with strong vertical confinement. T_1^e increases monotonically with ω_{\perp} . This is because, as we approach the spherical confinement regime ($\omega_z^e = \omega_{\perp}^e$), the Dresselhaus SOI of electrons is gradually suppressed.⁴⁰ No such trend is however observed for holes, as H_{BIA} does not cancel out even if the confinement is isotropic. As a matter of fact, T_1^h shows an evident non-monotonic behavior, with minimum at $\omega_{\perp} = 28$ meV and increasing away from it. It is worth noting that a previous study by Woods et al. predicted T_1^h to decrease with the QD diameter²⁹, while a similar study by Lu and co-workers for somewhat larger QDs predicted the opposite trend.³⁰ Fig. 2(a) shows that both predictions are conciliable, corresponding to the right and left sides of the T_1^h minimum, respectively. The origin of the different trends will be discussed in Section III B.

Figs. 2(b-c) show the spin lifetime dependence on the vertical confinement in QDs with moderately strong and weak lateral confinement, respectively. The confinement strengths roughly correspond to self-assembled^{46,47} and electrostatic⁴⁸ QDs. As can be seen in Fig. 2(b), electrons and holes have opposite behaviors. T_1^e now decreases with ω_z because the structure is becoming flatter (less isotropic). Instead, the behavior of T_1^h is similar to that observed for varying lateral confinement, with a shallow minimum at $\omega_z = 14$ meV. Previous studies have shown that T_1^h increases with the vertical confinement.³⁰ This is consistent with the right side of the T_1^h minimum in Fig. 2(b), but here we show that the opposite trend is also possible if the QD aspect ratio is large enough (left side of the minimum).

Fig. 2(c) illustrates the case in which the lateral confinement is weak. The minimum of T_1^h is now shifted towards very small $\hbar\omega_z$ values so that only the right side behavior is seen in the range under study. Interestingly, here T_1^h shows a clear saturation with increasing vertical confinement ($\hbar\omega_z > 40$ meV), which has not been noticed before.³⁰ As we show in Section III B, this saturation reflects the fact that H_{BIA} has replaced $hh-lh$ mixing as the main source of SOI.

The inset in Fig. 2(b) compares T_1^h in InAs and GaAs QDs with moderate lateral confinement. As can be observed, the spin lifetime in InAs QDs is longer than that in GaAs QDs when $\omega_z > \omega_{\perp}$, which is e.g. the case of self-assembled QDs. This is an unexpected result because the valence band SOI of InAs is stronger than that of GaAs.⁴¹ The underlying reason is that the Dresselhaus SOI interaction is stronger for GaAs (see b_{41} in Table I), and it provides a significant contribution to the total spin admixture.

Figure 2(d) shows the the spin-flip lifetime of electrons and holes in a self-assembled-like QD as a function of the spin splitting energy. For electrons, T_1^e is largely deter-

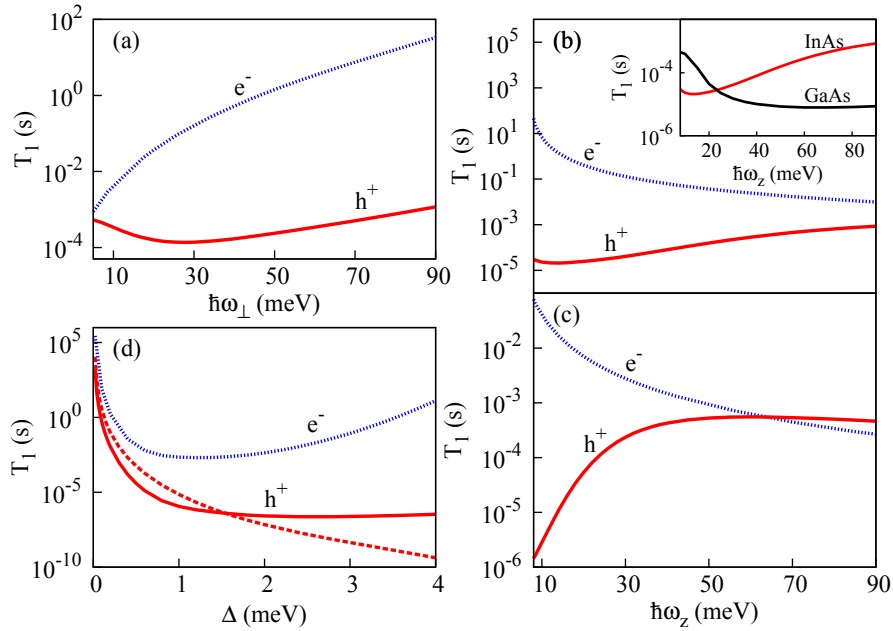


FIG. 2: Hole (solid line) and electron (dotted line) spin lifetime in InAs QDs, as a function of the lateral confinement (a), vertical confinement (b-c) and spin splitting energy (d). The inset in (b) compares T_1^h for InAs and GaAs. (a): $\hbar\omega_z^{hh} = 50$ meV, $\Delta = 0.4$ meV. (b): $\hbar\omega_{\perp}^{hh} = 20$ meV, $\Delta = 0.4$ meV. (c) $\hbar\omega_{\perp}^{hh} = 5$ meV, $\Delta = 0.4$ meV. (d): $\hbar\omega_{\perp}^{hh} = 20$ meV and $\hbar\omega_z^{hh} = 50$ meV.

mined by the efficiency of the carrier-phonon coupling.⁴⁰ It is short when the phonon wavelength is of the same order as the carrier wavefunction extension, but it increases for large (small) Δ values because the phonon wavelength becomes too short (long), as $q \approx \Delta/\hbar c$. The same happens for holes (notice that $G_{r,r'}(\mathbf{q})$ in Eq. (29) vanishes in the limits of large and small phonon wavevector). Yet, figure 2(d) shows that T_1^h is only sensitive to Δ for small splittings, but then it reaches a plateau where $T_1^h \sim \mu\text{s}$. The different behavior of holes and electrons is due to the different effective mass along the growth direction, m_z . For $\hbar\omega_z^{hh} = 50$ meV, the characteristic length of the oscillator states in the growth direction, $l_z = \sqrt{\hbar/m_z \omega_z}$, is $l_z^e = 4.5$ nm for electrons and $l_z^{hh} = 2.4$ nm for holes, i.e. the hole confinement is stronger. As a result, larger values of Δ are required for T_1^h to increase.

Experiments with excitons in self-assembled InGaAs QDs have revealed a negligible influence of e - h interactions on T_1^h .²⁴ Our results would be consistent with such a observation in the regime of large Δ . For self-assembled QDs, however, $\Delta \leq 0.5$ meV. Thus, the insensitivity noticed in the experiment is inconsistent with the single-phonon processes we consider. This suggests that two-phonon processes dominate in these systems.^{15,32} On the other hand, experiments with colloidal nanorods have shown a sizable increase of T_1^h when changing from type-I to type-II confinement, which modulates the e - h exchange energy from typical colloidal structure values (few meV) to type-II system values (fractions of meV).³⁶ We have run simulations for a nanorod-like geometry (dashed line in Fig. 2(d)) and find that the weak vertical confine-

ment renders T_1^h sensitive to Δ for all the range under study, in agreement with the experiment. This indicates that the weak vertical confinement of rods renders single-phonon processes efficient.

To close this section, we notice that previous theoretical studies have predicted that hole spin lifetimes can exceed those of electrons in very flat QDs.³¹ Fig. 2 shows that this could actually be achieved in gated structures, where lateral confinement is very weak (see the crossing between T_1^e and T_1^h in panel (c)). However, for typical self-assembled InAs QDs, T_1^e is about one order of magnitude longer than T_1^h (see panel (b) for large $\hbar\omega_z$).⁵⁰ This is consistent with experimental measurements by Heiss et al.²⁶

B. Mechanism of spin admixture

Spin admixture is a requirement for spin-flip transitions to take place.⁵¹ In this section, we compare the spin admixture resulting from all the SOI terms affecting the hole ground state. As we shall see, once the dominant SOI mechanism is determined, one can rationalize the geometry dependence of T_1^h described in the previous section. For convenience of the analysis, in what follows we plot and discuss relaxation rates, $1/T_1^h$.

Figure 3(a) shows the relaxation rate for the InAs QDs of Fig. 2(a), but now obtained by calculating hole states with the diagonal terms of H_L plus different SOI terms: off-diagonal H_L terms (hereafter hh - lh coupling), full Dresselhaus Hamiltonian (H_{BIA}), hh - lh coupling plus

linear-in- k term ($H_L + H_{C_k}$) and hh - lh coupling plus the dominant cubic-in- k Dresselhaus term ($H_L + H_{b41}$). The total rate, corresponding to $H_L + H_{BIA}$, is also shown (thick black line). One can see that H_L (red solid line) is more important than H_{BIA} (blue dashed line) for large ω_\perp values. However, as the lateral confinement is weakened and the system becomes flatter, H_{BIA} gains weight. For self-assembled QDs ($\hbar\omega_\perp \approx 10 - 25$ meV), H_{BIA} is already comparable to H_L and it becomes dominant for weakly confined (e.g. gated) QDs. Fig. 3 also reveals that the linear-in- k BIA term (gray dot-dashed line) is but a secondary mechanism, which barely enhances the relaxation rate coming from H_L . This is in spite of the fact that it is a source of direct admixture between hh states with opposite spin, with no participation of lh states. For this reason, it had been proposed as the dominant SOI term in flat QDs with weak lateral confinement.³⁵ Instead, most of the H_{BIA} contribution comes from the cubic-in- k b_{41} term (see green dotted line). This term relies on intermediate lh states in order to mix hh $J_z = +3/2$ and $J_z = -3/2$ components (see Eq. (A3) in the Appendix), which implies that a simultaneous description of hh and lh states is necessary for realistic modeling.

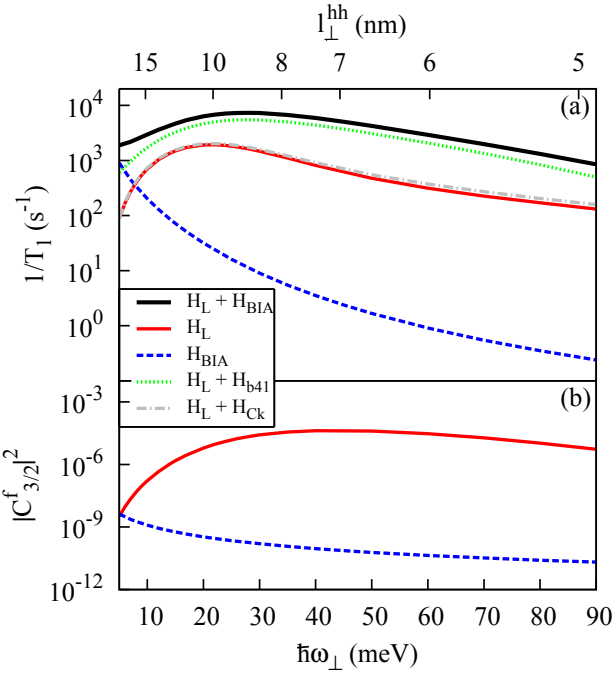


FIG. 3: Hole spin relaxation (a) and weight of the minor hh component (b) as a function of the lateral confinement. Different SOI terms are considered. The system is the same as that of Fig. 2(a).

By comparing the total relaxation rate coming from $H_L + H_{BIA}$ with that coming from H_L and H_{BIA} , it is clear that the total rate is not just the sum of the two independent mechanisms. For example, at $\hbar\omega_\perp = 30$ meV, adding H_{BIA} to H_L enhances $1/T_1^h$ about an order

of magnitude, even though the contribution coming from H_{BIA} alone is about 100 times smaller than that coming from H_L . Thus, simultaneously accounting for both SOI terms is also required for quantitative estimates.

For a qualitative understanding of the geometry dependence of $1/T_1^h$, we rewrite the hole states, Eq. (15), as $|\Psi_m^h\rangle = \sum_{J_z} c_{J_z}^m |\phi_{J_z}^m\rangle |3/2, J_z\rangle$, where $|\phi_{J_z}^m\rangle = \sum_r c_{J_z, r}^m |r\rangle$ is the envelope function associated with the periodic Bloch function $|3/2, J_z\rangle$. If we restrict to the diagonal components of H_{h-ph} , the matrix element determining the relaxation rate becomes:

$$\langle \Psi_f^h | \mathcal{H}_{h-ph}^{\lambda q} | \Psi_i^h \rangle \approx \sum_{J_z} (c_{J_z}^f)^* c_{J_z}^i \langle \phi_{J_z}^f | \mathcal{H}_{h-ph}^{\lambda q} | \phi_{J_z}^i \rangle. \quad (30)$$

When the QD is oblate or spherical, the low energy states are essentially hh states. Thus, the initial (final) state of the spin transition is mostly a pure spin up (spin down) hh state. Considering that $|c_{3/2}^i| \gg |c_{3/2}^f|$ ($|c_{-3/2}^f| \gg |c_{-3/2}^i|$), one can obtain an approximate expression:

$$\frac{1}{T_1^h} \propto \left| \langle \Psi_f^h | \mathcal{H}_{h-ph}^{\lambda q} | \Psi_i^h \rangle \right|^2 \propto |c_{3/2}^f|^2 \left| \langle \phi_{3/2}^f | \mathcal{H}_{h-ph}^{\lambda q} | \phi_{3/2}^i \rangle \right|^2. \quad (31)$$

In other words, the relaxation rate is proportional to the spin admixture of the ground state through the squared coefficient of the minor hh component (here spin up, $J_z = 3/2$), and proportional to the efficiency of the hole-phonon coupling through the rightmost matrix element.

The geometry dependence of $1/T_1^h$ for a given SOI mechanism simply reflects the spin admixture variation. This can be seen in Fig. 3(b), which shows that, for H_L and H_{BIA} , $|c_{3/2}^f|^2$ has the same qualitative dependence on the geometry as the corresponding $1/T_1^h$ values in Fig. 3(a). This allows us to interpret the observed maximum as a function of ω_\perp . For H_L , the spin admixture takes place necessarily through lh states, see Eq. (4). The weight of the minor hh component is related to the hh - lh coupling strength (through R and S operators in H_L) and to the energy splitting between the hh and intermediate lh states. The hh - lh coupling terms scale up with the confinement strength (note R and S operators dependence on k). In turn, the energy splitting, is largely influenced by the different masses of hh and lh . It is maximum for flat structures and goes to zero for slightly prolate structures.^{44,45} On the left side of Fig. 3, $\omega_\perp \ll \omega_z$, so lh states are far in energy. Changing ω_\perp has a weak effect on the energy splitting, which is mainly set by the lateral confinement. Then, the main effect of increasing ω_\perp is to enhance the hh - lh coupling strength, resulting in larger $|c_{3/2}^f|$ values. Around $\hbar\omega_\perp \approx 30$ meV, however, the lateral confinement energy becomes comparable to the vertical one. The lh states get close in energy and start participating in the admixture themselves, thus reducing the spin admixture

of the minor hh component.

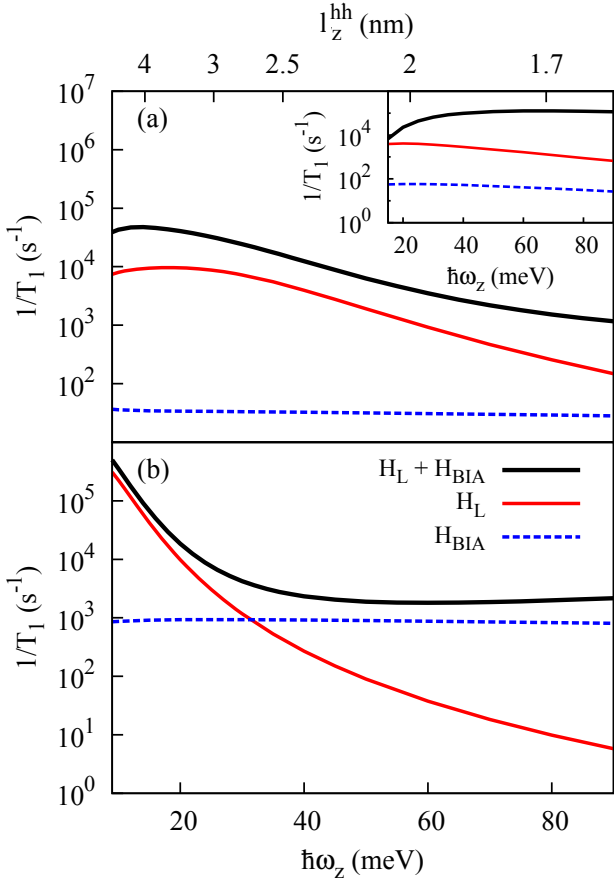


FIG. 4: Hole spin relaxation as a function of the vertical confinement. Different SOI terms are considered. (a): strong lateral confinement, $\hbar\omega_{\perp} = 20$ meV. (b): weak lateral confinement, $\hbar\omega_{\perp} = 5$ meV. The inset in (a) is the corresponding result for GaAs. The system is the same as that of Figs. 2(b) and (c).

Next, we analyze the mechanisms involved in the spin relaxation with varying vertical confinement. Figure 4 shows $1/T_1^h$ for the same systems as in Fig. 2(b-c), but calculating the hole states with the diagonal terms of H_L plus $hh-lh$ coupling (red solid line) or full H_{BIA} Hamiltonian (blue dashed line). Panel (a) corresponds to strong lateral confinement. The total rate has a maximum at $\hbar\omega_z = 14$ meV, whose origin is analogous to that described above for varying lateral confinement. Beyond the maximum, the total rate ($H_L + H_{BIA}$) decreases with the vertical confinement strength, in agreement with previous studies.³⁰ Yet, we also find that the decrease eventually saturates. This is evident for InAs QDs with weak lateral confinement, as shown in Fig. 4(b), or GaAs QDs with strong lateral confinement, as in Fig. 4(a) inset. The origin of this saturation is the contribution of H_{BIA} , which provides a lower bound to $1/T_1^h$. In particular, $H_{b_{41}}$ introduces off-diagonal coupling terms which

are quadratic in k_z (see operator L_{41} in the Appendix), instead of the linear k_z terms of H_L (see S operator in Eq. (4)). Since the uncoupled hh and lh energies are also quadratic in k_z , a perturbational analysis easily shows that the two contributions compensate each other. For strong ω_z , when lateral confinement is negligible, the cancellation is exact and the relaxation rate does not depend on the vertical confinement.

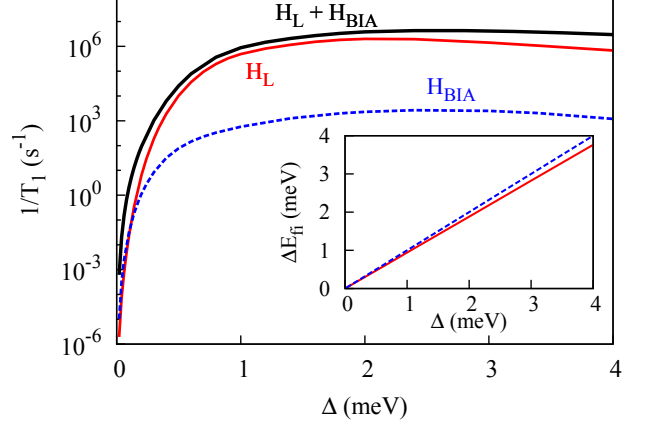


FIG. 5: Hole spin relaxation as a function of the spin splitting energy in a QD with $\hbar\omega_{\perp} = 20$ meV and $\hbar\omega_z = 50$ meV. Same legend as in Fig. 3 is used. The inset compares the energy splitting between the Kramer doublet for $hh-lh$ coupling and Dresselhaus SOI.

The magnitude of the spin splitting also influences the dominant mechanism of spin admixture. This is illustrated in Fig. 5, which considers a self-assembled InAs QD with varying spin splitting energy. For large Δ , H_L has a dominant contribution to the relaxation rate, but H_{BIA} becomes equally important for small enough Δ . The relative enhancement of the role of H_{BIA} originates in its zero-field spin splitting, which leads to larger energy difference between the Kramers pair (ΔE_{fi}) than with Δ alone, as shown in the figure inset. When $\Delta \rightarrow 0$ and the phonon wavelength increases beyond the QD size, the extra energy coming from the zero-field spin splitting of H_{BIA} provides a significant contribution to preserve the hole-phonon coupling efficiency.

C. Light hole spin relaxation

When the aspect ratio increases and the QD shape becomes prolate, the hole ground state evolves from the eminent hh character discussed so far to lh character, as noted e.g. in colloidal nanorods.⁴²⁻⁴⁵ Here we investigate how the change of the ground state affects the relaxation between the two highest hole states. Fig. 6(a) shows the hole energy levels in a QD with $\hbar\omega_{\perp} = 40$ meV as a function of $\hbar\omega_z$. In the limit of strong and weak vertical confinement, the two highest states are essentially hh and lh doublets, $J_z = \pm 3/2$ and $J_z = \pm 1/2$ respectively. In the intermediate regime, $\hbar\omega_z = 9 - 17$ meV, the two

doublets cross. This gives rise to pronounced changes in the relaxation rate, as shown in Fig. 6(b).

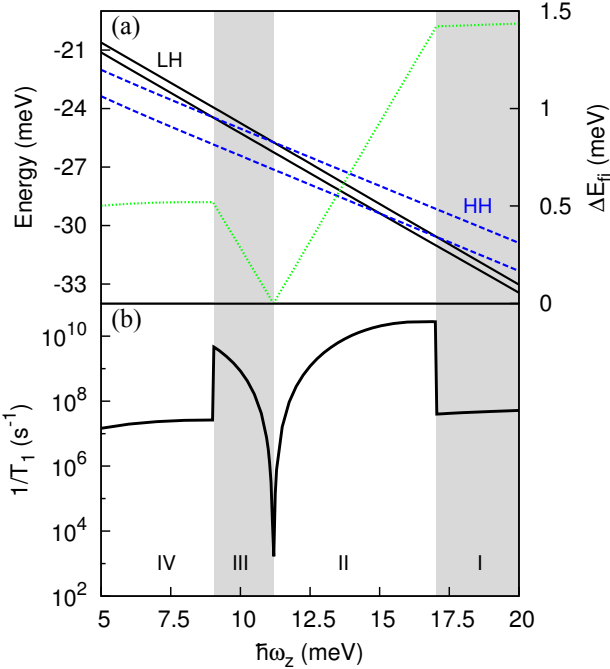


FIG. 6: Hole energy levels (a) and spin relaxation rate (b) around the hh - lh crossing region. $\hbar\omega_{\perp} = 40$ meV and $\Delta = 2$ meV. In (a), solid and dashed lines are used for states with dominant lh and hh character, respectively. The dotted line gives the energy splitting. Shaded are used to identify the regions with different kind of states involved in the transition.

The changes can be understood as follows. In region I of the figure, the two highest states are the hh doublet. The relaxation is between states with opposite spin and roughly constant energy splitting (see ΔE_{fi} , dotted line in Fig. 6(a)). At $\hbar\omega_z = 17$ meV, when we enter region II, the excited hh state crosses with the first lh state. Now the relaxation is between a lh ($J_z = -1/2$) and a hh ($J_z = -3/2$). Since lh have mixed spin up and spin down projections, there is no need for spin flip and the transition is much faster. This explains the abrupt increase of $1/T_1^h$. However, the energy splitting between the hh and lh becomes smaller with decreasing ω_z because of their different masses. As a result, at $\hbar\omega_z = 11$ meV, the lh replaces the hh as the ground state. Near the degeneracy point, $\hbar\omega_z = 11.2$ meV, ΔE_{fi} is so small that hole-phonon coupling becomes inefficient and the relaxation is strongly suppressed, but it increases again in region III for the same reasons as in region II. Finally, at $\hbar\omega_z = 9$ meV, the excited lh state crosses with the highest hh state. We thus enter region IV, where the transition takes place between two lh states with orthogonal Bloch functions, $|3/2, \pm 1/2\rangle$. J_z admixture mechanisms are necessary and the relaxation becomes slow. As a matter of fact, the spin relaxation timescale for transitions between lh states is similar to that between hh states, in spite of the fact that their Bloch functions contain mixed

spins.

D. Mechanism of hole-phonon coupling

Electron-acoustic phonon coupling in QDs is known to occur mainly through deformation potential interaction when the energy splitting is large ($\Delta E_{fi} \gtrsim 0.1$ meV) and through piezoelectric potential when it is small.⁵² In principle, for holes the situation may differ because the deformation potential Hamiltonian, Eq. (18), is formally different from that of electrons. To investigate this point, in this section we compare the role of the two kinds of carrier-phonon coupling mechanism for holes subject to varying effective magnetic fields.

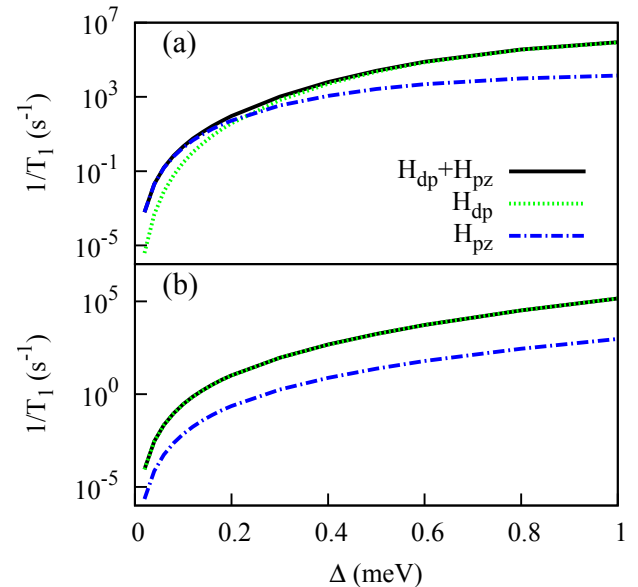


FIG. 7: Hole spin relaxation as a function of the spin splitting energy. (a): transition between hh states in a QD with $\hbar\omega_{\perp} = 20$ and $\hbar\omega_z = 50$ meV. (b): transition between lh states in a QD with $\hbar\omega_{\perp} = 40$ and $\hbar\omega_z = 5$ meV.

Figure 7(a) shows the spin relaxation rate in an oblate (quasi-2D) QD, where the highest states are hh , while Fig. 7(b) shows that in a prolate (quasi-1D) QD, where the highest states are lh . For the spin transition within the hh doublet, panel (a), the behavior is analogous to that of electrons. Deformation potential interaction (dotted line) provides the largest contribution to $1/T_1^h$ except for very small Δ , when piezoelectric interaction (dashed-dotted line) takes over. This is because all the terms of \mathcal{H}_{dp} are proportional to the phonon momentum \sqrt{q} , see Eqs. (25-27), while the piezoelectric potential is proportional to $1/\sqrt{q}$, see Eq. (24). With decreasing Δ both mechanisms become inefficient, because for long phonon wavelength $e^{i\mathbf{q}\mathbf{r}} \approx 1$. Then, in Eq. (29), the matrix element $G_{r,r'}(\mathbf{q}) \approx \langle r' | r \rangle$, i.e. it tends to the overlap between the envelope components of the initial and final states. For hh , these components have different symme-

tries, so the coupling vanishes. For example, in axially symmetric structures, the $J_z = +3/2$ component of the initial state has a well defined azimuthal angular momentum $m_z = 0$, which couples through the s^λ operator of H_{dp} with the $J_z = +1/2$ component of the final state, for which $m_z = -2$.⁵³

The situation for lh is quite different. As shown in Fig. 7(b), now deformation potential interaction is the dominant relaxation channel even for small Δ . The underlying reason is that, in contrast to the hh case, the off-diagonal terms of \mathcal{H}_{dp} couple envelope components with the same symmetry. For example, the $J_z = +3/2$ and $J_z = +1/2$ components of the initial and final state now have both $m_z = -1$, and hence are not orthogonal. As a consequence, $G_{r,r'}(\mathbf{q})$ does not vanish when $q \rightarrow 0$.

IV. SUMMARY

We have investigated hole spin relaxation in InAs and GaAs QDs using 3D 4-band $k\cdot p$ Hamiltonians. We have shown that the hole spin lifetime has a non-monotonic dependence on the lateral and vertical confinement strength. This is due to the interplay between the energy splitting of hh and lh , which is set by their different masses, and the anisotropic hh - lh coupling terms. The resulting geometry dependence of hole spin relaxation is qualitatively different from that of electrons.

hh - lh coupling and Dresselhaus SOI have been found to have comparable contributions to the spin admixture of hole states in self-assembled QDs, with the former becoming dominant for prolate structures, such as nanorods, and the latter for strongly oblate ones, such as gated QDs. The cubic-in- k Dresselhaus term leads to an upper bound of T_1^h with increasing vertical confinement, which is missed when considering hh - lh coupling only.

The spin relaxation between hh and lh is very fast because lh states have strong spin admixture. Instead, spin transitions between lh states with different Bloch angular momentum J_z take place in similar time scales as those between hh states with orthogonal spin. The main difference is that, for lh , deformation potential is the principal hole-phonon interaction mechanism even for small energy splittings.

Acknowledgments

Support from MICINN project CTQ2011-27324, UJI-Bancaixa project P1-1A2009-03, the Ramon y Cajal program (JIC) and UJI fellowship (CS) is acknowledged.

Appendix A: Dresselhaus Hamiltonian for Holes

In this appendix we write the explicit matrix forms of the different H_{BIA} terms in cartesian coordinates. Separating the different invariants in Eq. (9) we obtain:

$$H_{BIA} = H_{C_k} + H_{b_{41}} + H_{b_{51}} + H_{b_{52}}, \quad (A1)$$

where:

$$H_{C_k} = C_k \begin{pmatrix} 0 & -\frac{k_-}{2} & k_z & -\frac{\sqrt{3}k_-}{2} \\ -\frac{k_+}{2} & 0 & \frac{\sqrt{3}k_+}{2} & -k_z \\ k_z & \frac{\sqrt{3}k_-}{2} & 0 & -\frac{k_-}{2} \\ -\frac{\sqrt{3}k_+}{2} & -k_z & -\frac{k_+}{2} & 0 \end{pmatrix}, \quad (A2)$$

with $k_\pm = k_x \pm i k_y$.

$$H_{b_{41}} = b_{41} \begin{pmatrix} \frac{3}{2}P_{41} & \frac{\sqrt{3}}{2}L_{41} & 0 & 0 \\ \frac{\sqrt{3}}{2}L_{41}^\dagger & \frac{1}{2}P_{41} & L_{41} & 0 \\ 0 & L_{41}^\dagger & -\frac{1}{2}P_{41} & \frac{\sqrt{3}}{2}L_{41} \\ 0 & 0 & \frac{\sqrt{3}}{2}L_{41}^\dagger & -\frac{3}{2}P_{41} \end{pmatrix}, \quad (A3)$$

where $P_{41} = (k_x^2 - k_y^2)k_z$ and $L_{41} = i k_- k_x k_y - k_+ k_z^2$.

$$H_{b_{42}} = b_{42} \begin{pmatrix} \frac{27}{8}P_{41} & \frac{7\sqrt{3}}{8}L_{41} & 0 & -\frac{3}{4}L_{42} \\ \frac{7\sqrt{3}}{8}L_{41}^\dagger & \frac{1}{8}P_{41} & \frac{5}{2}L_{41} & 0 \\ 0 & \frac{5}{2}L_{41}^\dagger & -\frac{1}{8}P_{41} & \frac{7\sqrt{3}}{8}L_{41} \\ -\frac{3}{4}L_{42}^\dagger & 0 & \frac{7\sqrt{3}}{8}L_{41}^\dagger & -\frac{27}{8}P_{41} \end{pmatrix}, \quad (A4)$$

where $L_{42} = i k_+ k_x k_y + k_- k_z^2$.

$$H_{b_{51}} = b_{51} \begin{pmatrix} 0 & -\frac{\sqrt{3}}{4}K_+ & \frac{\sqrt{3}}{2}K_z & -\frac{3}{4}K_- \\ -\frac{\sqrt{3}}{4}K_- & 0 & \frac{3}{4}K_+ & -\frac{\sqrt{3}}{2}K_z \\ \frac{\sqrt{3}}{2}K_z & \frac{3}{4}K_- & 0 & -\frac{\sqrt{3}}{4}K_+ \\ -\frac{3}{4}K_+ & -\frac{\sqrt{3}}{2}K_z & -\frac{\sqrt{3}}{4}K_- & 0 \end{pmatrix}, \quad (A5)$$

where $K_+ = K_x + i K_y$, $K_- = K_x - i K_y$, $K_x = k_x (k_y^2 + k_z^2)$, $K_y = k_y (k_x^2 + k_z^2)$, and $K_z = k_z (k_x^2 + k_y^2)$.

$$H_{b_{52}} = b_{52} \begin{pmatrix} 0 & -\frac{\sqrt{3}}{4}M_+ & \frac{\sqrt{3}}{2}k_z^3 & -\frac{3}{4}M_- \\ -\frac{\sqrt{3}}{4}M_- & 0 & \frac{3}{4}M_+ & -\frac{\sqrt{3}}{2}k_z^3 \\ \frac{\sqrt{3}}{2}k_z^3 & \frac{3}{4}M_- & 0 & -\frac{\sqrt{3}}{4}M_+ \\ -\frac{3}{4}M_+ & -\frac{\sqrt{3}}{2}k_z^3 & -\frac{\sqrt{3}}{4}M_- & 0 \end{pmatrix}, \quad (A6)$$

where $M_+ = k_x^3 + i k_y^3$ and $M_- = k_x^3 - i k_y^3$.

* Electronic address: josep.planelles@uji.es

¹ J. Fischer, M. Trif, W. A. Coish, and D. Loss, Solid State

Commun. **149**, 1443 (2009).

² B. D. Gerardot, D. Brunner, P. A. Dalgarno, P. Öhberg,

S. Seidl, M. Kroner, K. Karrai, N. G. Stoltz, P. M. Petroff, and R. J. Warburton, *Nature (London)* **451**, 441 (2008).

³ D. Brunner, B. D. Gerardot, P. A. Dalgarno, G. Wüst, K. Karrai, N. G. Stoltz, P. M. Petroff, and R. J. Warburton, *Science* **325**, 70 (2009).

⁴ P. Fallahi, S. T. Yilmaz, and A. Imamoglu, *Phys. Rev. Lett.* **105**, 257402 (2010).

⁵ E. A. Checkhovich, A. B. Krysa, M. S. Skolnick, and A. I. Tartakovskii, *Phys. Rev. Lett.* **106**, 027402 (2011).

⁶ B. Eble, C. Testelin, P. Desfonds, F. Bernardot, A. Balocchi, T. Amand, A. Miard, A. Lemaitre, X. Marie, and M. Chamarro, *Phys. Rev. Lett.* **102**, 144601 (2009).

⁷ C. Testelin, F. Bernardot, B. Eble, and M. Chamarro, *Phys. Rev. B* **79**, 195440 (2009).

⁸ K. De Greve, P. L. McMahon, D. Press, T. D. Ladd, D. Bispin, C. Schneider, M. Kamp, L. Worschech, S. Hofling, A. Forchel, and Y. Yamamoto, *Nat. Phys.* **7**, 872 (2011).

⁹ T. M. Godden, J. H. Quilter, A. J. Ramsay, Y. Wu, P. Brereton, S. J. Boyle, I. J. Luxmoore, J. Puebla-Nunez, A. M. Fox, and M. S. Skolnick, *Phys. Rev. Lett.* **108**, 017402 (2012).

¹⁰ A. Greilich, S. G. Carter, D. Kim, A. S. Bracker, and D. Gammon, *Nat. Photonics* **5**, 703 (2011).

¹¹ P. Szumniak, S. Bednarek, B. Partoens, and F. M. Peeters, *Phys. Rev. Lett.* **109**, 107201 (2012).

¹² C. Y. Hsieh, R. Cheriton, M. Korkusinski, and P. Hawrylak, *Phys. Rev. B* **80**, 235320 (2009).

¹³ J. C. Budich, D. G. Rothe, E. M. Hankiewicz, and B. Trauzettel, *Phys. Rev. B* **85**, 205425 (2012).

¹⁴ R. Roloff, T. Eissfeller, P. Vogl, and W. Pötz, *New J. Phys.* **12**, 093012 (2010).

¹⁵ Y.-H. Liao, J. I. Climente, and S. J. Cheng, *Phys. Rev. B* **83**, 165317 (2011).

¹⁶ H. Kurtze, D. R. Yakovlev, D. Reuter, A. D. Wieck, and M. Bayer, *Phys. Rev. B* **85**, 195303 (2012).

¹⁷ K. Kowalik, O. Krebs, A. Lemaitre, J. A. Gaj, and P. Voisin, *Phys. Rev. B* **77**, 161305(R) (2008).

¹⁸ V. M. Huxter, J. Kim, S. S. Lo, A. Lee, P. Sreekumari Nair, and G. D. Scholes, *Chem. Phys. Lett.* **491**, 187 (2010).

¹⁹ T. Lundstrom, W. Schoenfeld, H. Lee, and P. M. Petroff, *Science* **286**, 2312 (1999).

²⁰ M. Reischle, G. J. Beirne, R. Rossbach, M. Jetter, and P. Michler, *Phys. Rev. Lett.* **101**, 146402 (2008).

²¹ S. D. Li, Y. J. Fu, and C. Cheng, *Opt. Express.* **20**, 19850 (2012).

²² E. Tsitsishvili, and H. Kalt, *Phys. Rev. B* **82**, 195315 (2010).

²³ K. Gündogdu, K. C. Hall, E. J. Koerperick, C. E. Pryor, M. E. Flatté, and T. F. Boggess, *Appl. Phys. Lett.* **86**, 113111 (2005).

²⁴ K. C. Hall, E. J. Koerperick, T. F. Boggess, O. B. Shchekin, and D. G. Deppe, *Appl. Phys. Lett.* **90**, 053109 (2007).

²⁵ S. Laurent, B. Eble, O. Krebs, A. Lemaitre, B. Urbaszek, X. Marie, T. Amand, and P. Voisin, *Phys. Rev. Lett.* **94**, 147401 (2005).

²⁶ D. Heiss, S. Schaeck, H. Huebl, M. Bichler, G. Abstreiter, J. J. Finley, D. V. Bulaev, and D. Loss, *Phys. Rev. B* **76**, 241306(R) (2007).

²⁷ F. Fras, B. Eble, P. Desfonds, F. Bernardot, C. Testelin, M. Chamarro, A. Miard, and A. Lemaitre, *Phys. Rev. B* **86**, 045306 (2012).

²⁸ R. Winkler, *Spin-Orbit Coupling Effects in Two-Dimensional Electron and Hole Systems*, (Springer, Berlin, 2003).

²⁹ L. M. Woods, T. L. Reinecke, and R. Kotlyar, *Phys. Rev. B* **69**, 125330 (2004).

³⁰ C. Lü, J. L. Cheng, and M. W. Wu, *Phys. Rev. B* **71**, 075308 (2005).

³¹ D. V. Bulaev, and D. Loss, *Phys. Rev. Lett.* **95**, 076805 (2005).

³² M. Trif, P. Simon, and D. Loss, *Phys. Rev. Lett.* **103**, 106601 (2009).

³³ H. Wei, M. Gong, G. C. Guo, and L. He, *Phys. Rev. B* **85**, 045317 (2012).

³⁴ K. Roszak, V. M. Axt, T. Kuhn, and P. Machnikowski, *Phys. Rev. B* **76**, 195324 (2007).

³⁵ E. Tsitsishvili, R. V. Baltz, and H. Kalt, *Phys. Rev. B* **72**, 155333 (2005).

³⁶ J. He, H. Zhong, and G. D. Scholes, *Phys. Rev. Lett.* **105**, 046601 (2010).

³⁷ J. M. Luttinger, *Phys. Rev. B* **102**, 1030 (1956)

³⁸ See e.g. page 97 of L. C. L. Y. Voon, and M. Willatzen, *The k-p Method*, (Springer, Berlin, 2009).

³⁹ T. Uenoyama, and L. J. Sham, *Phys. Rev. B* **42**, 7114 (1990).

⁴⁰ J. Planelles, J. I. Climente, and C. Segarra, *J. Phys. Chem. C* **116**, 25143 (2012).

⁴¹ I. Vurgaftman, J. R. Meyer, and L. R. Ram-Mohan, *J. Appl. Phys.* **89**, 5815 (2001).

⁴² J. Hu, L. S. Li, W. Yang, L. Manna, L. W. Wang, and A. P. Alivisatos, *Science* **292**, 2060 (2001).

⁴³ D. Katz, T. Wzansky, O. Millo, E. Rothenberg, T. Mokari, and U. Banin, *Phys. Rev. Lett.* **89**, 086801 (2002).

⁴⁴ L. C. L. Y. Voon, R. Melnik, B. Lassen, and M. Willatzen, *Nano Lett.* **4**, 289 (2004).

⁴⁵ J. Planelles, F. Rajadell, and J. I. Climente, *J. Phys. Chem. C* **114**, 8337 (2010).

⁴⁶ J. H. Blokland, F. J. P. Wijnen, P. C. M. Christianen, U. Zeitler, and J. C. Maan, *Phys. Rev. B* **75**, 233305 (2007).

⁴⁷ R. J. Warburton, B. T. Miller, C. S. Dürr, C. Bödefeld, K. Karrai, J. P. Kotthaus, G. Medeiros-Ribeiro, P. M. Petroff, and S. Huant, *Phys. Rev. B* **58**, 16221 (1998).

⁴⁸ G. J. Schinner, J. Repp, E. Schubert, J. P. Kotthaus, A. K. Rai, D. Reuter, A. D. Wieck, A. O. Govorov, and A. W. Holleitner, *arXiv:1204.3199*.

⁴⁹ O. Madelung, *Semiconductors: Data Handbook*, (Springer, Berlin, 2004).

⁵⁰ The same conclusions, albeit with somewhat lower T_1^e , are obtained using larger electron masses to account e.g. for Ga diffusion into the InAs QD.

⁵¹ A. V. Khaetskii, and Y. V. Nazarov, *Phys. Rev. B* **64**, 125316 (2001).

⁵² J. I. Climente, A. Bertoni, G. Goldoni, and E. Molinari, *Phys. Rev. B* **74**, 035313 (2006).

⁵³ In axially symmetric systems, the envelope functions of the Luttinger spinor have well defined z-component of the orbital angular momentum, $m_z = F_z - J_z$. In oblate QDs, the highest doublet has $F_z = \pm 3/2$, and in prolate QDs it has $F_z = \pm 1/2$. See e.g. Ref. 45.